A discrete forcing method dedicated to moving bodies in two-phase flow

William Benguigui, Antoine Doradoux, Jérôme Laviéville, Stephane Mimouni, Elisabeth Longatte

A Discrete Forcing Method dedicated to moving bodies in two-phase flow.

W. Benguigui[1,2], A. Doradoux[3,4], J. Lavieville[1], S. Mimouni[1], E. Longatte[2]

[1] *Fluid Mechanics, Energy and Environment Department, EDF R&D, 6 Quai Watier, 78400 Chatou, France*
[2] *IMSIA, UMR EDF/CNRS/CEA/ENSTA 9219, Universit Paris-Saclay, 91762 Palaiseau, France*
[3] *Naval Group, Technopole de la Mer, 83190 Ollioules, France*
[4] *IMB, UMR CNRS 5251, Universit de Bordeaux, 351 cours de la libration, 33405 Talence, France*

The numerical simulation of interaction between structures and two-phase flows is a major concern for many industrial applications. In order to address this challenge, the motion of structures has to be tracked accurately. In the present work, a discrete forcing method based on a porous medium approach is proposed to follow non-deformable rigid body with an imposed velocity by using a finite-volume Navier-Stokes solver code dedicated to multi-phase flows and based on a two-fluid approach. To deal with the action reaction principle at the solid wall interfaces in a conservative way, a porosity is introduced allowing to locate the solid and insuring no diffusion of the fluid-structure interface. The volumetric fraction equilibrium is adapted to this novelty. Mass and momentum balance equations are formulated on a fixed cartesian grid. Interface tracking is addressed in detail going from the definition of the porosity to the changes in the discretization of the momentum balance equation. This so-called Time and Space Dependent Porosity (TSDP) method is then validated by using analytical and elementary test cases.

Received . . .

KEY WORDS: Fluid-structure interface tracking method, multi-phase flow, CFD, Discrete Forcing method, Two-fluid approach

1. INTRODUCTION

In industrial applications such as petroleum, nuclear industry, or naval engineering, mobile solid bodies in two-phase flows are a major concern as they might be involved in different possible damages. Consequently, several points of view can be considered to investigate them through experiments or numerical simulations. For the purpose of this work, numerical simulation is considered.

In Computational Fluid Dynamics (CFD), to deal with moving-boundary problems, it is possible to use mobile-mesh methods such as the Arbitrary Lagrangian Eulerian[21] or Chimera [1]. Mobile-mesh methods are very accurate since the mesh is body-fitted at anytime. However, the issue of this

*Correspondence to: Email: william.benguigui@edf.fr

kind of method is the high computational cost of mesh updating for complex geometries. Immersed Boundary methods are more and more popular since the mesh generation is simple and not updated.

Based on the original approach introduced by Peskin 1972 [22], Immersed Boundary Method (IBM) consists in representing fluid in an Eulerian framework and solid in a Lagrangian one. The domain contains the structure, it is considered as a real part of the calculation domain. The main advantage with this method is in the non-explicit representation of the structure, such that it is possible to perform calculations on complex geometries using Cartesian grids. Mittal and Iaccarino [19] categorized IBM into two approaches:

- Continuous forcing: the operator discretization is unchanged, a source term is added in the momentum balance equation in order to take into account the immersed boundary. Penalty method and Peskin approach are continuous forcing methods.
- Discrete forcing: operator discretization is different close to the fluid-structure interface in order to take into account the boundary. The challenge of these methods is to properly reconstruct the interface properties.

In the present work, a Discrete Forcing method dedicated to moving bodies in two-phase flow is proposed. The concept of these methods, in mirror of continuous forcing ones, is to keep unchanged the conservation laws at the wall by modifying the operator discretization in order to have the right condition at the interface. For example, the Cut-cell approach [5, 29]modifies the shape of the control volumes near the interface by cutting and merging them. Mass, convective, diffusive fluxes and gradients have to be computed on each face of these new cells. Developed by Tseng et al. [25], the Ghost-Fluid approach consists in the introduction of a force in Navier-Stokes equation in order to impose the exact boundary condition at the interface. For each cell crossed by the interface, a ghost zone is introduced in the non-fluid area where the boundary condition has to be enforced. These methods are robust and used for different situations from bubbly flow to fluid-structure interaction. Bai et al. [2] used Cartesian cut cell approach to simulate waves for example. However, in the present work, we are interested in moving-bodies in two-phase flows. This is not the first time an article is dedicated to this kind of flow with a discrete-forcing method. For example, Xie [28] investigated breaking waves, he used the cut-cell method to reproduce the reef. Most of the time these methods are implemented in multi-phase flow code based on a one-fluid approach. The novelty of this article is to implement a discrete forcing method in a code based on a two-fluid approach and to adapt the volumetric fraction equilibrium and the momentum balance equation to it.

Based on a porous media approach, the Time and Space Dependent Porosity is a discrete forcing approach able to track non-deformable solids with imposed velocities in a multi-phase flow on a Cartesian grid. In order to reconstruct the wall, several major steps are required such as the convection of the porosity, reshaping cells taking into account the fluid-structure interface or computing a fitted pressure gradient. Firstly, two-phase flow governing equations and modeling are presented. Then, a discrete forcing method based on a porous media approach and dedicated to follow a structure in a two-phase flow is proposed. Variable interface-reconstructions are detailed. In order to assess the proposed novelties, four verification test cases are presented: Poiseuille flow with porous walls, cylinder moving in a fluid with the same velocity, accelerated piston, and one based on Taylor-Green vortices. Finally, two-phase flow applications are presented with the Time and Space Dependent Porosity method: a suddenly stopped cylinder in a fluid, the impact of a bubble on a cylinder, a dam break on a wet bed, and a wave generator.

2. TWO-PHASE FLOW MODELING

The present work involves a CFD code dedicated to multiphase flows and based on the two-fluid (extended to n) approach. NEPTUNE_CFD code developed in the framework of the NEPTUNE project [11] (funded by EDF, CEA, Framatome and IRSN) is a finite-volume code with a collocated arrangement for all variables. The data structure is totally face-based, which allows the use of arbitrary shaped cells (tetrahedra, hexahedra, prisms, pyramids, ...). Using a pressure correction approach [13], it is able to simulate multiphase flows by solving a set of three balance equations for

each field. These balance equations are deduced from volumetric averaging of local instantaneous balance equations where the k-phase volumetric fraction is written α_k. In multiphase flow, one property of the k-phase volumetric fractions is:

$$\sum_{k=1}^{N} \alpha_k = 1 \tag{1}$$

with N the number of fluid phases included into the fluid domain.

Fields can represent different kinds of multiphase flows. The present work is focusing on liquid-gas flows only and restricted to adiabatic cases, simplifying the system to the mass and momentum balance equations for each phase k:

$$\begin{aligned} \frac{\partial(\alpha_k \rho_k)}{\partial t} + \underline{\nabla} \cdot (\alpha_k \rho_k \underline{U_k}) &= 0 \\ \frac{\partial (\alpha \ \rho \ \underline{U_k})}{\partial t} + \underline{\nabla} \cdot (\alpha_k \rho_k \underline{U_k} \underline{U_k}) &= -\alpha_k \underline{\nabla P} + \alpha_k \rho_k \underline{g} + \underline{\nabla} \cdot \overline{\overline{\tau}}_k + \sum_{p=1 \ p \neq k}^{N} \underline{M}_{p \to k} \end{aligned} \tag{2}$$

where α, ρ, $\underline{U}$, Γ, P, τ, $\underline{g}$ and $\underline{M}$ are respectively the volume fraction, the density, the velocity, the mass transfer, the pressure, the Reynolds-stress tensor, the gravity and the momentum transfer to the phase k. Depending on the forms of the same physical components, i.e.: a continuous or dispersed field, the interfacial momentum transfers of each phase are defined. Different approaches are consequently possible depending on the two-phase flow regime. For a bubbly flow, a dispersed approach for the gas field is more appropriate [18]. However, for stratified or slug flow, a Large Interface approach seems to be more suitable [6]. To deal with multi-regime flow, where small and large bubbles are present, both models using respectively two and three fields are implemented: the Generalized Large Interface To Dispersed approach [17] and the multi-field approach [8].

3. TIME AND SPACE DEPENDENT POROSITY METHOD DEFINITION

The aim of discrete forcing methods is to strictly ensure the conservation laws at the close vicinity of the interface. The idea is to reshape the cells crossed by the interface and to build specific schemes inside them. The interface is approximated as a plane in each cut-cell. The domain contains the structure, which is considered as a real part of the calculation domain. A recognition function is therefore required to determine the solid location on the cells. The main advantage of these methods lies in the non-explicit representation of the structure, such as, it is possible to perform calculations on complex geometries using Cartesian grids. The major challenge of these methods is to reconstruct the interface properties.

In order to locate the solid, cells are identified as a solid, fluid, or interface cells. In the present method, the whole domain is considered in the framework of a porous media approach where a time and space dependent fraction called porosity is 0 in the solid, and 1 in the fluid. The fluid-structure interface is consequently represented with a porosity between 0 and 1. Here, the porosity is as follows:

$$\varepsilon(\underline{x}, t) = 1 - \alpha_s(\underline{x}, t) \tag{3}$$

with α the volumetric fraction of the solid phase, and $\varepsilon(\underline{x}, t)$ the porosity (in $\underline{x}$ at time t) being between $[0, 1]$. Therefore, the previous relation (1) describing the volumetric fraction balance becomes:

$$\sum_{k} \alpha_k(\underline{x}, t) = \varepsilon(\underline{x}, t) \tag{4}$$

This method involves a non-moving Cartesian grid where the body is meshed and defined with a porosity equal to 0 insuring no mass transfer between solid and fluids. In a finite-volume framework, the porosity is computed for a cell I by using the following relation:

$$\varepsilon_I = \frac{\text{fluid volume of the cell } I}{\text{total volume of the cell } I}. \tag{5}$$

Here, the solid motion is tracked thanks to the porosity evolution in a Lagrangian framework. To take into account the solid motion and the presence of an interface in cut-cells, the porosity has to be convected and the momentum balance equations are formulated differently.

3.1. Porous mass balance equation and media definition

The time and space dependent porosity definition is the key element in the method. The volume of the solid domain should be constant whether the object is moving or not. Acting like volumetric fraction, a porosity is computed for each cell and for each face of the domain in order to convect the structure.

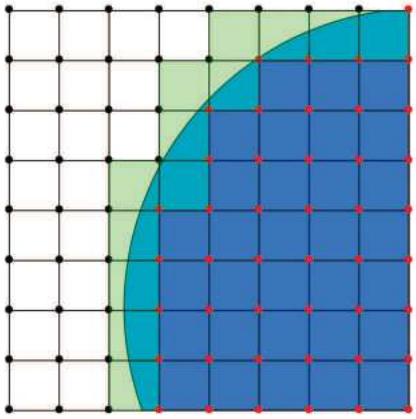

Figure 1. *Cell-porosity computation: nodes in the solid domain are in red, others in black. In a cell, if each node is solid (blue), it is a solid-cell; if each node is not solid (white), it is a fluid-cell; otherwise it is a a cut-cell (green).*

3.1.1. Cell-porosity computation For each cell, three kinds of cells are possible and defined thanks to the porosity:

1. if the cell is solid, porosity value is 0 ;
2. if the cell is fluid, porosity value is 1 ;
3. in other cases, the cell contains an interface.

At each time step, the porosity is computed by using a Volume of Fluid Initialization (VOFI) method [3, 4] as follows. An implicit function f is introduced. This function is defined as follows : $f(x, y, z) = 0$ with x, y,and z defining a point located on the interface between the fluid domain and the solid domain. Then, this function is used in order to evaluate in each cell the porosity. Examples of cells with porosity of 0, 1 and intermediate values are displayed on Figure 1.

3.1.2. Geometric face-porosity determination If a face is cut by the fluid-structure interface, the two Cartesian neighboring cells sharing this face are required to compute geometrically the face porosity. Based on the node coordinates and the porosity of each cell, it is determined geometrically by assuming the interface straight (linear function) and not curved. Several configurations are possible and illustrated in two dimensions in Figure 2 for $\varepsilon_I > \varepsilon_J$.

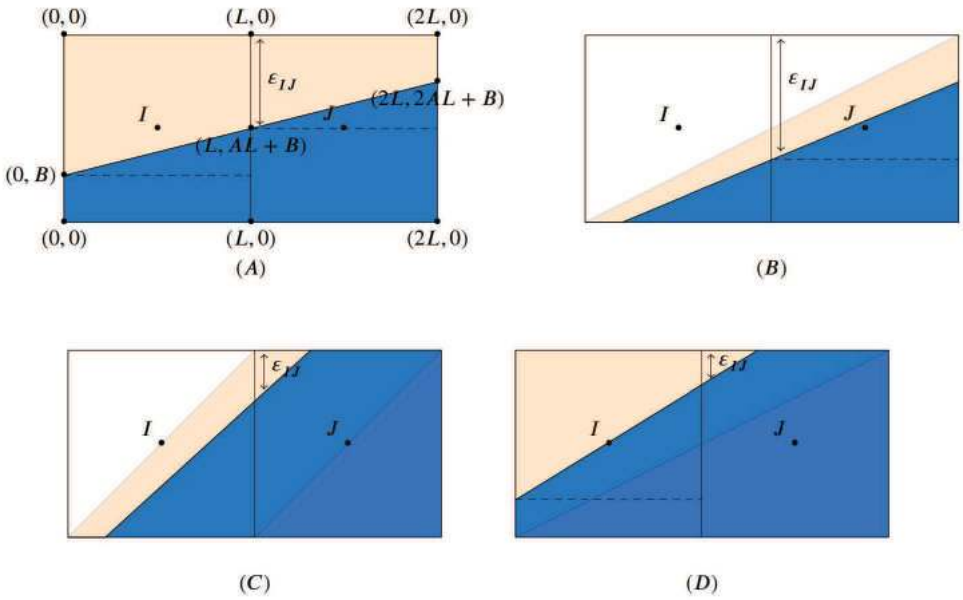

Figure 2. *Fluid-structure interface crossing a face in a two-dimensional configuration. Each cell area is calculated by using triangle and rectangle areas when it is required.*

The interface is defined: $y = Ax + B$ where A and B are two real coefficients. In each cell, the blue surface is computed based on node coordinates, A, B. Consequently, for a given case :

$$\begin{cases} S_I = 1 - \alpha_I = s_1(A, B, x) \\ S_J = 1 - \alpha_J = s_2(A, B, x) \end{cases} \tag{6}$$

where S and S designate respectively the blue areas of both cells, s_i and s_j are two functions computing the area based on A, B and x. The computation of this system leads to an evaluation of A and B, and then ε_{IJ}. For example, node coordinates are given in Figure.2 for case (A). Based on them, the blue surface is computed in each cell such as:

$$\begin{cases} S_I = 1 - \alpha_I = BL + AL^2/2 \\ S_J = 1 - \alpha_J = (AL + B)L + AL^2/2 \end{cases} \tag{7}$$

Then, by solving the present system, A and B are computed. Finally, $\varepsilon_{IJ} = 1 - (AL + B)$. For three-dimensional cases, the mesh is assumed enough refined to use exactly the same method.

3.1.3. Convected porosity computation As described in (4): the porosity has to be treated like k-phase volumetric fractions, hence convecting the porosity is necessary. There are no mass transfer between a solid and other phases, therefore:

$$\frac{\partial \varepsilon}{\partial t} + \nabla \cdot (\varepsilon \underline{U_s}) = 0 \tag{8}$$

with $\varepsilon = \sum_k \alpha$. In a finite-volume framework, the discretization at each time step is given by:

$$\frac{\varepsilon_I^{n+1} - \varepsilon_I^n}{\Delta t} \Omega_I + \sum_{J \in N_I} \varepsilon_{IJ}^n \phi_{IJ} = 0 \tag{9}$$

with $\phi_{IJ} = \underline{U_s} \cdot \underline{n}_{IJ}$, where $\underline{n}_{IJ}$ is the face unit normal vector between cells I and J, and N_I neighboring cells around I. For multiple solids, the domain is decomposed in subdomains depending

on the position of each structure in order to differentiate their own velocities like in Figure 3. In order to allow the independent motion of different structures with several velocities, the solid volumetric phase fraction $\alpha_s = 1 - \varepsilon$ is convected since it is null outside each structure. The convection equation becomes:

$$\frac{{\alpha_s}_I^{n+1} - {\alpha_s}_I^{n}}{\Delta t}\Omega_I + \sum_{J \in N_I} ({\alpha_s}_{IJ}^{n} - 1)\phi_{IJ} = 0. \tag{10}$$

Outside structures, one gets $\sum_{J \in N_I} \phi_{IJ} = 0$. Given that α_s is also null outside solid sub-domains, the convection equation is thus formulated in an equivalent way in order to keep the minimum and the maximum principles true:

$$\frac{{\alpha_s}_I^{n+1} - {\alpha_s}_I^{n}}{\Delta t}\Omega_I + \sum_{J \in N_I} ({\alpha_s}_{IJ}^{n} - {\alpha_s}_I^{n})\phi_{IJ} = 0. \tag{11}$$

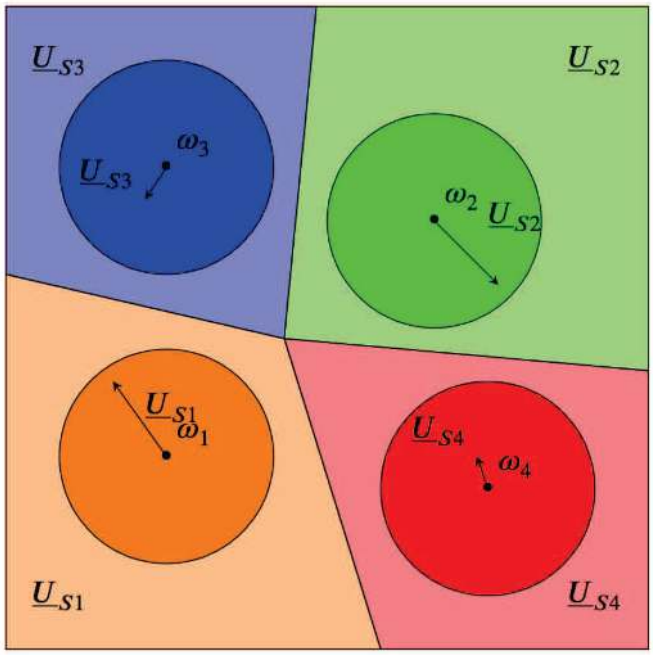

Figure 3. *Decomposition of the domain according to the position of each cylinder. In each subdomain, the solid velocity is taken equal to the corresponding solid.*

To minimize the numerical diffusion and keep positivity and maximum principles for porosity, a θ-scheme is used to define the face porosity fraction, and each time step is subdivided in sub-time step to approximate accurately the face porosity. An example of 2D configuration is given in Fig.4. Using a θ-scheme, the porosity is expressed in terms of the current face function α_{sGEOM} and a decentered value $\alpha_{sUPWIND}$ as follows :

$$\alpha_{sIJ} = \theta_{IJ}\alpha_{sIJ}^{GEOM} + (1 - \theta_{IJ})\alpha_{sIJ}^{UPWIND} \tag{12}$$

Using an upwind decentered scheme yields : $\alpha_{sIJ}^{UPWIND} = \alpha_{sI}$ for $\phi_{IJ} > 0$ $= \alpha_{sJ}$ for $\phi_{IJ} < 0$. $\alpha_{sIJ}^{UPWIND} \in [0, 1]$. As far as possible, θ_{IJ} is close to 1 in order to preserve the highest geometric contribution. The UPWIND and geometric face porosity computation are satisfied thanks to a Courant condition on the time step. Introducing the time step subdivision, let i be an integer $i \in [0, i_{max}]$ and β the solid fraction during a sub-iteration such

that $\beta_I = \alpha_I$ and $\beta_I^{i_{max}} = {\alpha_s}_I^{n+1}$. The sub-cycling time step becomes: $dt = \frac{\Delta t}{i_{max}}$. Therefore, the to define β_{IJ}^i and leads to the $\alpha_{s_{IJ}}^n$ thanks to the relation:

$$\alpha_{s_{IJ}}^n = \frac{\sum_{i\in[0,i_{max}]} \beta_{IJ}^i}{i_{max}}. \tag{13}$$

This relation is used to solve iteratively the mass balance equation (11). The derivation of the

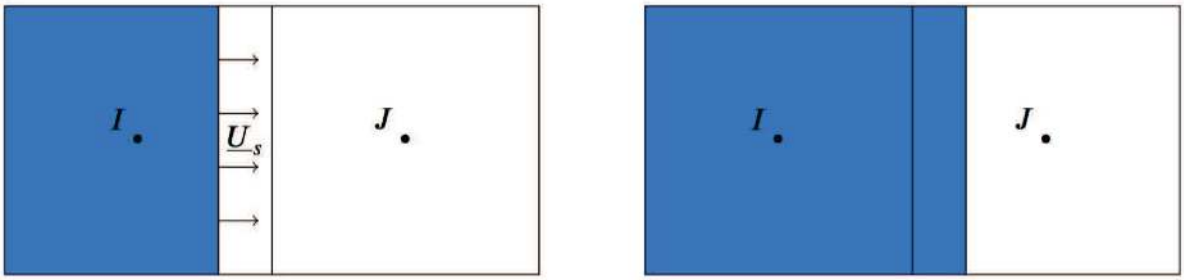

Figure 4. *Fluid-structure interface crossing a cell face. Sub-cycles are required in this case to approximate step by step the value of the face-porosity.*

is presented below. For a cell I, lets assume $0 \leq \beta_I^i \leq 1$ and derive $0 \leq \beta_I^{i+1} \leq 1$:

1. **Positivity**

$$\frac{\beta_I^{i+1} - \beta_I^i}{dt}\Omega_I + \sum_{J\in N_I} (\beta_{IJ}^i - \beta_I^i)\phi_{IJ} = 0$$

It is possible to formulate the expression by highlighting decentered terms according to the flux sign:

$$\frac{\beta_I^{i+1} - \beta_I^i}{dt}\Omega_I + \sum_{J\in N_I, \phi_{IJ}\geq 0} (\theta_{IJ}\beta_{IJ}^{i,GEOM} + (1-\theta_{IJ})\beta_I^i - \beta_I^i)\phi_{IJ})$$

$$+ \sum_{J\in N_I, \phi_{IJ}<0} (\theta_{IJ}\beta_{IJ}^{i,GEOM} + (1-\theta_{IJ})\beta_J^i - \beta_I^i)\phi_{IJ}) = 0$$

One defines $A = -\sum_{J\in N_I, \phi_{IJ}<0}(\theta_{IJ}\beta_{IJ}^{i,GEOM} + (1-\theta_{IJ})\beta_J^i)\phi_{IJ})$ which is positive.

$$\frac{\beta_I}{dt}\Omega_I = \frac{\beta_I^i}{dt}\Omega_I + A + \sum_{J\in N_I, \phi_{IJ}<0} \beta_I\phi_{IJ} - \sum_{J\in N_I, \phi_{IJ}\geq 0} \theta_{IJ}(\beta_{IJ}^{i,GEOM} - \beta_I^i)\phi_{IJ}$$

he positivity of β_I^{i+1}, the condition is:

$$\sum_{J\in N_I, \phi_{IJ}\geq 0} \theta_{IJ}(\beta_{IJ}^{i,GEOM} - \beta_I^i)\phi_{IJ} \leq \frac{\beta_I^i}{dt}\Omega_I + A + \sum_{J\in N_I, \phi_{IJ}<0} \beta_I\phi_{IJ} \tag{14}$$

2. Let assume $\beta_I^{i+1} = 1 - \varepsilon_I^{i+1}$. To ensure the positivity of ε_I^{i+1} (consequently $\beta_I \leq 1$), the condition is similarly:

$$\sum_{J\in N_I, \phi_{IJ}\geq 0} \theta_{IJ}(\varepsilon_{IJ}^{i,GEOM} - \varepsilon_I^i)\phi_{IJ} \leq \frac{\varepsilon_I^i}{dt}\Omega_I + A + \sum_{J\in N_I, \phi_{IJ}<0} \varepsilon_I\phi_{IJ} \tag{15}$$

Therefore, θ has to ensure both conditions. θ_{IJ} is defined per cell (not per face) as a θ_I. Thus, the conditions become for a cell I:

$$\begin{cases} \theta_{I,1} \leq \dfrac{\frac{\beta_I^i}{dt}\Omega_I + A + \sum_{J\in N_I,\phi_{IJ}<0}\beta_I\phi_{IJ}}{\sum_{J\in N_I,\phi_{IJ}\geq 0}(\beta_{IJ}^{i,GEOM}-\beta_I^i)\phi_{IJ}} \\ \theta_{I,2} \leq \dfrac{\frac{\varepsilon_I^i}{dt}\Omega_I + A + \sum_{J\in N_I,\phi_{IJ}<0}\varepsilon_I\phi_{IJ}}{\sum_{J\in N_I,\phi_{IJ}\geq 0}(\varepsilon_{IJ}^{i,GEOM}-\varepsilon_I^i)\phi_{IJ}} \end{cases} \tag{16}$$

First, as the priority is the geometric part of β_{IJ}, θ_I has to be maximum:

$$\begin{cases} \theta_{I,1} = \dfrac{\frac{\beta_I^i}{dt}\Omega_I + A + \sum_{J\in N_I,\phi_{IJ}<0}\beta_I\phi_{IJ}}{\sum_{J\in N_I,\phi_{IJ}\geq 0}(\beta_{IJ}^{i,GEOM}-\beta_I^i)\phi_{IJ}} \\ \theta_{I,2} = \dfrac{\frac{\varepsilon_I^i}{dt}\Omega_I + A + \sum_{J\in N_I,\phi_{IJ}<0}\varepsilon_I\phi_{IJ}}{\sum_{J\in N_I,\phi_{IJ}\geq 0}(\varepsilon_{IJ}^{i,GEOM}-\varepsilon_I^i)\phi_{IJ}} \end{cases} \tag{17}$$

To satisfy both conditions with one value of θ_I, the minimum has to be taken between $\theta_{I,1}$ and $\theta_{I,2}$. As these conditions have to be true for all cell around, consequently the θ_I has to satisfy conditions from all cells around, therefore:

$$\theta_I = MIN(\theta_k, \theta_I) = MIN(\theta_k, MIN(\theta_{I,1}, \theta_{I,2})) \tag{18}$$

with $k \in N$. To determine A in each cell, its minimum is taken in order to not overestimate the maximum value of θ_I. Consequently:

$$A = \sum_{J\in N_I,\phi_{IJ}<0} MIN(\beta_{IJ}^{GEOM}, \beta_J)\phi_{IJ} \tag{19}$$

3.2. Momentum balance equation

3.2.1. Geometric parameter definitions To express the presence of a fluid-structure interface in a cell, one requirement is to define structure geometric parameters: structure unit normal vector and interface center of gravity. The interface is consequently considered as a new face in each cell.

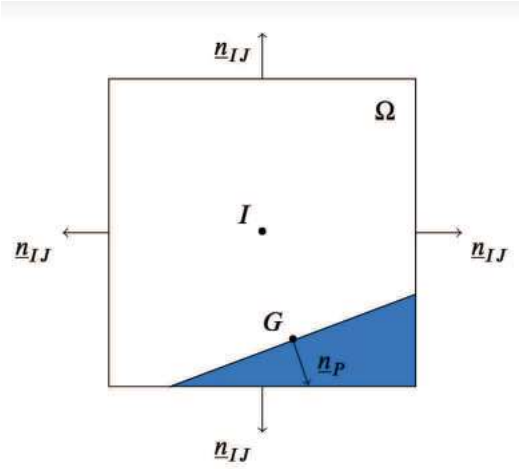

Figure 5. Cell crossed by the fluid-structure interface, geometric characteristics re-shaping.

Figure 5 represents a crossed-cell in 2D, where G is the interface center of gravity, and $\underline{n_p}$ the structure unit normal vector. For a fully fluid cell, the following relation is satisfied:

$$\sum_{J \in N_I} \underline{n}_{IJ} = 0 \tag{20}$$

Consequently, for the interface cell presented in Figure 5, based on the different face porosities, the relation becomes:

$$\sum_{J \in N_I} \varepsilon_{IJ} \underline{n}_{IJ} + \underline{n}_p = 0 \tag{21}$$

Then, G is defined as the solid face center of gravity. According to the finite volume discretization, it can be expressed as :

$$\varepsilon_I \Omega = \sum_{J \in N_I} \varepsilon_{IJ} \underline{x}_{G_{IJ,k}} . \underline{n}_{IJ,k} + \underline{x}_{G_P,k} . \underline{n}_{P,k} \tag{22}$$

with x the face centers of gravity and $k = x,\ y$ or z. From (22), G coordinates are obtained.

When the volume of the cell is reduced because of the structure, cell centers of gravity are recomputed depending on the solid face (like in cut-cell methods [5, 29]). For a fully solid cell, the velocity is $\underline{U}$. But, for a cut-cell, the velocity is the fluid one taking into account the presence of the solid and its motion. According to the diffusion theorem, the center of gravity of a fully fluid cell is written:

$$i_G = \frac{1}{\Omega} \sum_{J \in N_I} \frac{i_{IJ}^2}{2} S_{IJ,i} \tag{23}$$

with $i = x,\ y,\ z$. Therefore, for a cut-cell like in Figure 6, the porosity ε_I is taken into account:

$$i_G = \frac{1}{\varepsilon_I \Omega} \sum_{J \in N_I} \frac{i_{IJ}^2}{2} S_{IJ,i} \tag{24}$$

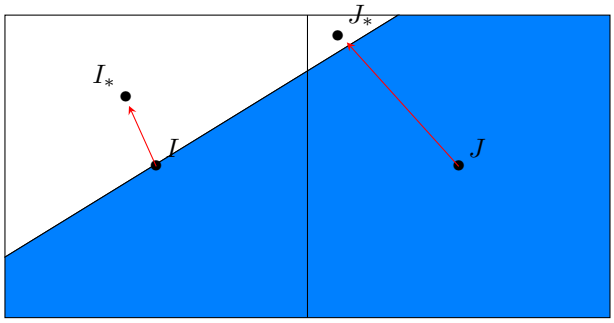

Figure 6. Sketch of the cell center displacements.

3.2.2. Pressure field A diffusion equation is solved inside the solid by taking into account the dual of a Dirichlet boundary condition as:

$$\nabla^2 P = 0 \text{ with } P = P_{fluid} \text{ at the fluid-structure interface.} \tag{25}$$

Initially, for a regular Cartesian grid, for two cells I and J, the pressure at the face joining them is given by:

$$P_{IJ} = \frac{1}{2}(P_I + P_J). \tag{26}$$

Based on displaced cell centers of gravity (Figure 5), the face pressure is computed with a geometric ponderation between P_I and P_J at the intersection between the face and IJ. Consequently, the approximation of pressure computed at the face is improved since it depends on the position of each cell center of gravity around.

The pressure gradient reconstruction is required at the fluid-structure interface in order to not disturb the flow around the structure. Based on the displaced cell center of gravity computed previously, it is possible to write for an intersected cell I:

$$P_G = P_I + \underline{IG}.\underline{\nabla P_I}. \tag{27}$$

Using finite-volume method, the pressure gradient is written:

$$\int_{\Omega_I} \nabla P_I d\Omega = \sum_{J \in N_I} \varepsilon_{IJ} P_{IJ} \underline{n}_{IJ} + P_G \underline{n}_p. \tag{28}$$

As,

$$\sum_{J \in N_I} \varepsilon_{IJ} \underline{n}_{IJ} + \underline{n}_p = 0 \tag{29}$$

this yields the implicit formula:

$$\underline{\nabla P_I} \varepsilon_I \Omega = \sum_{J \in N_I} \varepsilon_{IJ} (P_{IJ} - P_I) \underline{n}_{IJ} - \sum_{J \in V_I} \varepsilon_{IJ} (\underline{IG_P}.\underline{\nabla P_I}) \underline{n}_{IJ}. \tag{30}$$

3.2.3. Diffusive terms According to the finite-volume discretization, for a cell I, the diffusion term without the wall contribution is written as:

$$\sum_{J \in N_I} \alpha_{IJ} \mu_{IJ} \frac{\underline{U}_J - \underline{U}_I}{IJ} \mid\mid \underline{n}_{IJ} \mid\mid . \tag{31}$$

with α the phase face volumetric fraction between I and J.

To take into account the additional face, the diffusion term in I is projected on the fluid-structure interface characterized by $\underline{n_P}$.

$$\alpha_I \mu_I \frac{\underline{U}_P - \underline{U}_I}{IP} \mid\mid \underline{n}_P \mid\mid . \tag{32}$$

Here, $\underline{U}$ is defined as the cell velocity projected on the wall, and according to the solid velocity with a non-slip condition:

$$\underline{U_P} = (\underline{U_{solid}}.\underline{n_P}).\underline{n_P} + \underline{U_I} - (\underline{U_I}.\underline{n_P}).\underline{n_P}. \tag{33}$$

Finally, the diffusion term for a cut-cell I is written as:

$$\sum_{J \in V_I} \alpha_{IJ} \mu_{IJ} \frac{\underline{U}_J - \underline{U}_I}{IJ} \mid\mid \underline{n}_{IJ} \mid\mid + \alpha_I \mu_I \frac{\underline{U}_P - \underline{U}_I}{IP} \mid\mid \underline{n}_P \mid\mid . \tag{34}$$

4. ROBUSTNESS OF THE METHOD

In order to evaluate the previously-mentioned Time and Space Dependent Porosity method, it is necessary to validate it. Some of the configurations used to assess its consistency are given below.

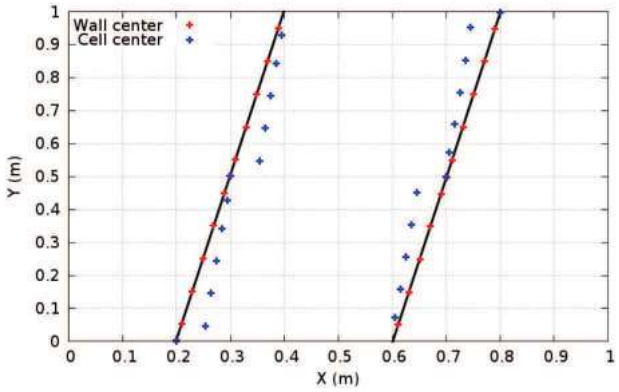

Figure 7. *Geometric points representation for an inclined channel.*

4.1. Test cases with no motion

4.1.1. Single-phase flow in an inclined channel The configuration involves a square domain representing a channel conveying a single-phase flow. In the context of the TSDP method, the channel walls are described by the porosity. The flow enters into the channel with a given inclination. Several inclinations are tested. This elementary configuration is chosen because an analytical formulation of the solution is available for comparison with numerical results. The square dimensions are 1mx1m. Several two-dimensional grid refinements are considered.

First, with a 10x10x1 mesh, the center of gravity from the solid faces and the new cell centers of gravity are computed for an inclined channel in Figure 7. The grid is represented in black dash and the walls in black. Their computation has been validated for different cases such as a cylinder for example. Then, several channel inclinations are computed to check the validity of the proposed novelties defined previously and the interface reconstruction for a Poiseuille flow with wall crossing cells (geometric parameters are fully used). Thanks to the different stated changes, results are in agreement with analytical solutions for different inclinations. The L^2 relative error is computed for

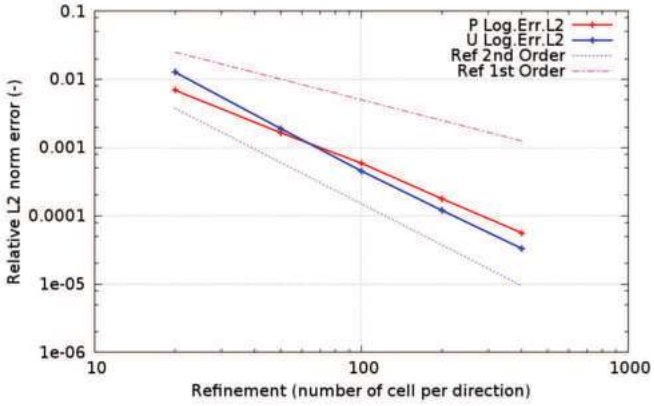

ure 8. *Poiseuille flow: L^2 relative error and order conservation graphics.*

pressure, and velocity. Based on five mesh refinements, it attests the order conservation despite the time and space porosity method implementation: 1.60 for pressure and 1.95 for velocity.

4.1.2. Taylor-Green vortices around an immersed body The configuration involves a square domain containing Taylor-Green vortices with an immersed square solid in the center where a slip condition is ensured at its walls. Therefore as shown in Figure 9 the vortices are not disturbed in this area.

Domain borders have periodic conditions. The theoretical flow is characterized by flow velocity components u and u_y in both space directions x and y of the form :

$$\begin{cases} u_x(x,y,t) = -cos(\pi x)sin(\pi y)e^{-2\pi^2\mu t} \\ u_y(x,y,t) = sin(\pi x)cos(\pi y)e^{-2\pi^2\mu t} \end{cases} \tag{35}$$

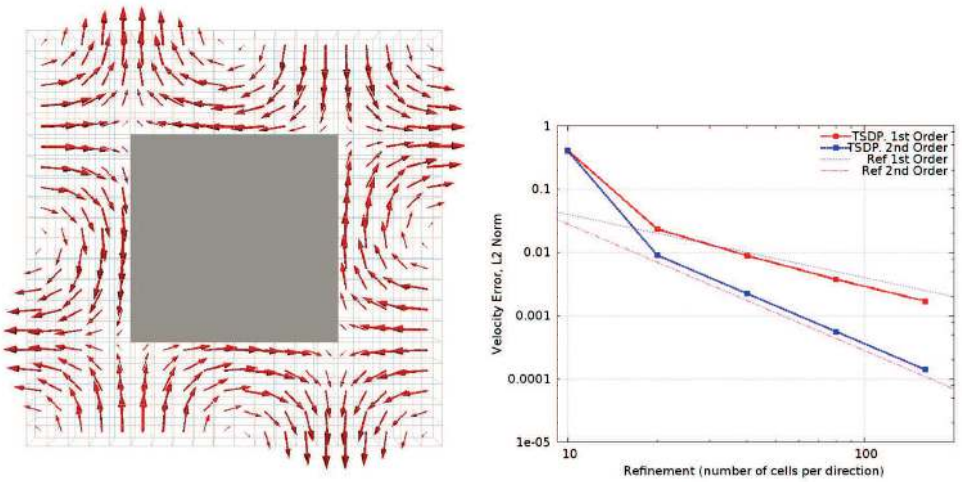

Figure 9. *Sketch (left) of the Taylor-Green vortices around an immersed square solid with slip walls and numerical results for 5 grid refinements (right).*

The single-phase fluid flow is assumed to be incompressible. 5 grid refinements are considered in this case. The fluid-structure interface does not cross any cells, consequently porosity in the domain is 1 or 0. This choice reduces the approximation done when the structure has an angle in one cell. This case highlights the correct reconstruction of a wall with slip condition, and the correct implementation of the method which does not affect the order conservation. In Figure 9, the L^2 relative error for velocity is plotted depending on the grid refinement. It is possible to see that the coarse mesh is too coarse to follow the vortices. Then, for the others, depending on the chosen algorithm, the order conservation is ensured.

4.1.3. Laminar wake of a cylinder, $Re = 40$ A non-moving cylinder is considered immersed in a flow with a Reynolds number of 40. In this case, the flow at the wake of the cylinder is stable and creates two symmetric recirculation zones as displayed in Fig.10.

A cylinder having a diameter $D = 1\ m$ and a center $(4, 7.5)$ is immersed in a domain $[0, 15m][0, 15m]$ discretized such as $\Delta x = \Delta y = 0.05\,m$. The inlet velocity of the fluid is $1\ m/s$. The Reynolds number is 40.

The force acting on the cylinder is computed with cells having a porosity between 0 and 1 (cut cells) by using the pressure and velocity gradient at wall :

$$\mathbf{F} = \oint \mathbf{n}(-P\overline{\overline{I}} + \mu(\overline{\overline{\nabla \mathbf{U}}} + \overline{\overline{\nabla^T \mathbf{U}}}))dS \tag{36}$$

Then, the drag and lift coefficients are defined by:

$$C_D = \frac{F_x}{\frac{1}{2}\rho U_0^2 D} \qquad C_L = \frac{F_y}{\frac{1}{2}\rho U_0^2 D} \tag{37}$$

In Tab.1, the present method is in agreement with different other referenced works for each characteristics variables. The correct wall reconstruction is therefore assessed.

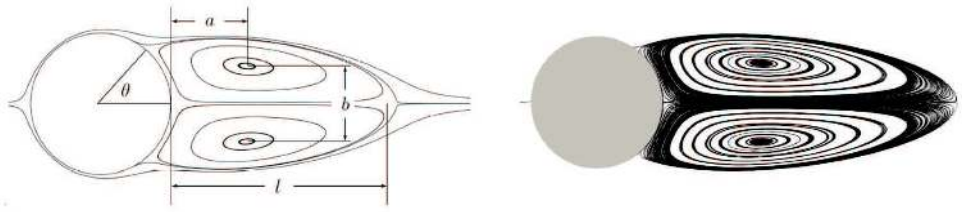

Figure 10. *Definition of the characteristic wake dimensions for the steady flow over a stationary circular cylinder (left) and numerical streamlines for* $Re = 40$.

	l/D	a/D	b/D	θ	C_D
=					
Tritton (1959)* [24]	-	-	-	-	1.59
Coutanceau & Brouard (1977)* [7]	2.13	0.76	0.59	53.8	-
Taira & Colonius (2007) [23]	2.30	0.73	0.60	53.7	1.54
Wang & Zhang (2011) [27]	2.36	0.72	0.6	53.8	1.54
Present study	2.25	0.746	0.597	53.7	1.56

Table I. *Comparison between experimental results (with an "*"), other simulations and the present study for a cylinder at* $Re = 40$.

4.2. Test cases with motion

4.2.1. One dimensional body The case of an incompressible flow and a solid animated by a constant acceleration in a one dimensional channel of length $10m$ using 4 grid refinements is considered. In the fluid, the momentum balance equation gives $\frac{\partial u}{\partial t} = -\nabla p$, consequently this case allows to assess the validity of the pressure gradient computation when cell are recovered or discovered by the solid, since it is given by the solid acceleration. Moreover, it demonstrates the capacity of the θ-scheme to provide the correct face porosity.

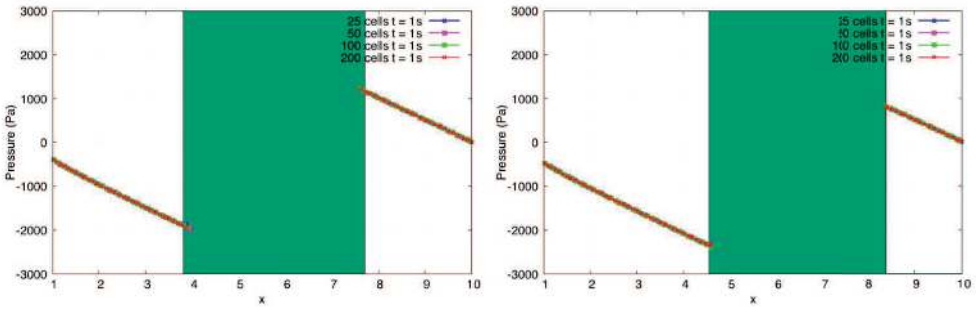

Figure 11. *Pressure profile after discovering a cell (accelerating solid) after 1s (left) and 2s (right). The solid is in green.*

On Figure 11, for an acceleration of $0.5m/s^2$, after 1s and 2s, with 4 mesh refinements, the Time and Space Dependent Porosity method predicts the correct pressure since the slope is 0.5.

4.2.2. Cylinder moving at fluid velocity In a square domain 2mx2m, cylinder and fluid(s) have the same velocity $u_x = 0.1m/s$ and $u_y = 0.1m/s$ such as: For an incompressible flow, the pressure must remain at its initial value. In the present study, the initial condition is $P_{domain} = 0\ Pa$.

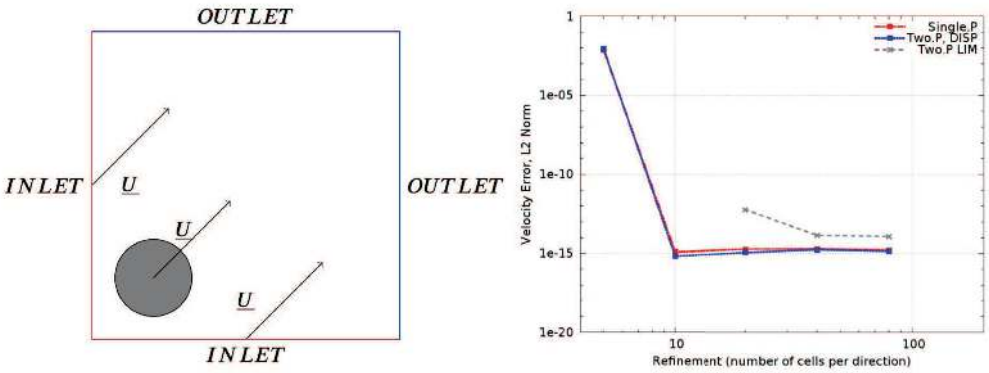

Figure 12. *Geometry of cylinder at fluid velocity case (left) and velocity error for a cylinder at fluid velocity in single and two-phase flow (with 2 approaches : dispersed and continuous), (right).*

Moreover, the velocity must remain unchanged. The aim is to validate the convection of the porosity using single then two-phase flow. In fact, this case does not work if the porosity is not convected.

In Figure 12, with 5 mesh refinements, results are presented in terms of L^2-norm error for velocity in single phase-flow, dispersed-flow ($\alpha = 10\%$) and Large Interface model (liquid-gas interface between (0,0) and (2,2)). Only 3 mesh refinements are presented with the Large Interface model since the interface recognition function needs 5 cells.

The first mesh, having only 5 cells in each direction, is obviously too coarse. For the other, with any approach, it is possible to see that the error is extremely low. From the second refinement, the mean pressure in the domain is always under $10^{-12}\ Pa$.

4.3. Applications of the Time and Space Dependent Porosity method

Some applications of the method are here presented:

1. a cylinder moving in a fluid at rest at $Re = 40$ and suddenly stopped,
2. bubble impact on a cylinder,
3. a dam break on a wet bed,
4. a paddle oscillating on a free surface.

Numerical simulations are here performed in single or two-phase flow with moving body. The displacement is still imposed by the user.

4.3.1. Suddenly stopped cylinder Based on Koumoutsakos & Leonard (1995) [15], 2D numerical simulation of cylinder instantaneously moving and stopped for a laminar Reynolds number of 40 is performed. The cylinder is moving with a constant velocity during 5 seconds in a fluid at rest, and stopped at $t = 5\ s$. During 10 seconds, drag coefficients around the cylinder are recorded. The geometry of the case is reported in Figure 13.

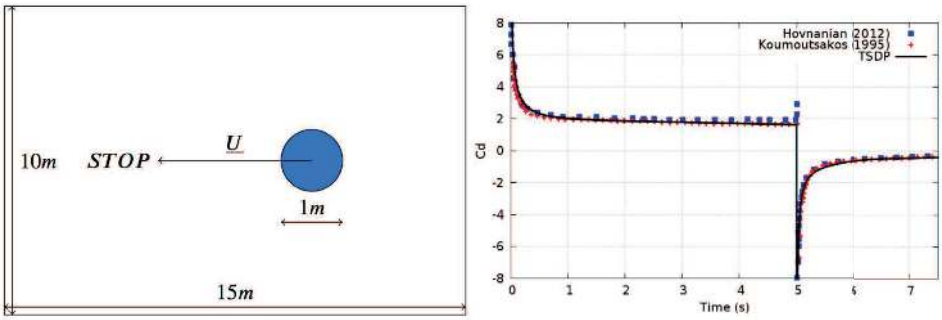

Figure 13. *Geometry of the cylinder suddenly stopped case (left) and drag coefficient around the cylinder moving with* $Re \quad 40$ *and suddenly stopped. Numerical results are compared with other methods [15, 12] (right).*

As the Reynolds number is low, only the laminar part of the velocity gradient is relevant. The wall pressure is detected thanks to the pressure gradient with a first order development. Consequently, the global drag coefficients are in agreement over time. In Fig.13, at $t = 5s$, it is possible to see on the drag coefficient tendency a strong change which is the results of the cylinder velocity becoming 0.

A slight discrepancy may be seen at $t = 5s$ with other results, otherwise they are in a reasonable agreement. In Figure 14, isolines of vorticity at 8 different instants are presented from the numerical simulation (left) and from the experiment (right). First column is dedicated to instant before the stop and the second to after. Obviously, the isolines represented are in excellent agreement with experimental data.

4.3.2. Bubble impact on a cylinder The present 3D-application is a comparison between a computation utilizing a body-fitted mesh and another one utilizing the Time and Space Dependent Porosity. In Figure.15, the fluide is at rest. The large cylinder represents a solid obstacle and the small one a bubble. The bubble goes up thanks to gravity.

The fully-developed regime gives a bubble Reynolds number of 3.57, an Eötvos number of 116 and a Morton number of 266. The gas is air and the liquid has the following properties: $\rho = 1350\ kg/m^3$, $\mu = 2.02\ Pa.s$, and $\sigma = 0.0785\ N.m$. The liquid is at rest and the gravity is $9.81\ m/s$. A fully cartesian mesh is used with $\Delta x = \Delta y = \Delta z = 0.6mm$. To body-fit the cylinder, cells crossed by the cylinder or inside it are removed, then border nodes are extrapolated on the cylinder. Hence, for both cases a cartesian grid is used. However, for the standard case, the cells are not strictly cartesian since their node are moved to fit the cylinder.

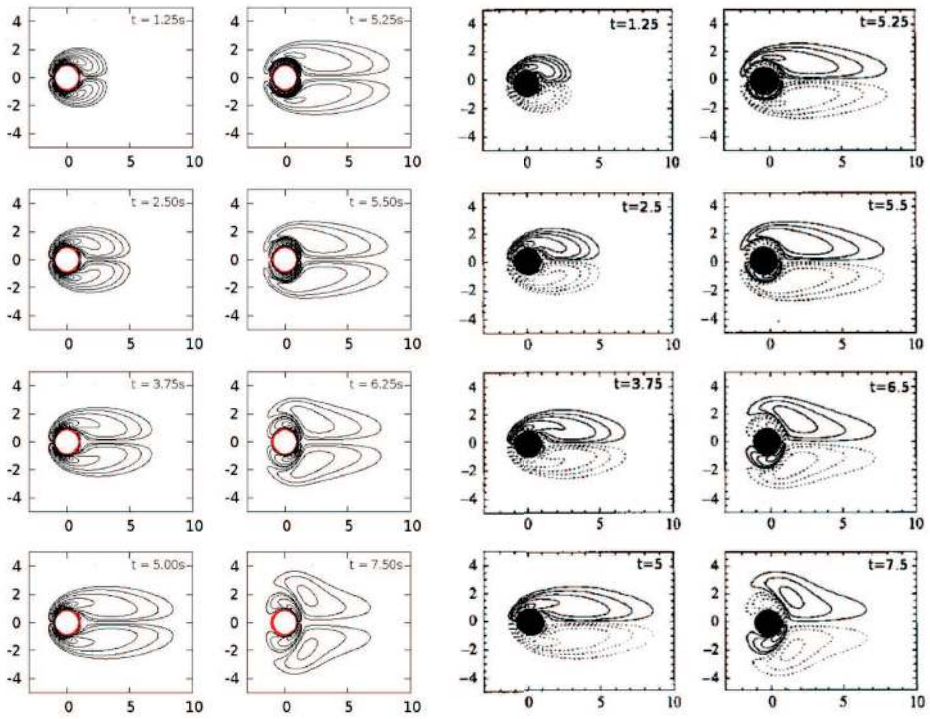

Figure 14. *Vorticity isolines for 8 different times with numerical simulation (left) and experimental data (right) from [15]*

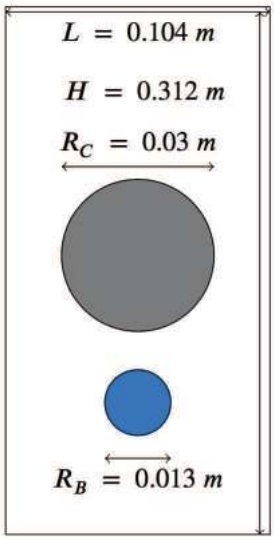

Figure 15. *Geometry of the bubble impact on a cylinder case.*

The present study is realized with the Large Interface model to follow the bubble. Drag and surface tension forces from [9] are applied to the gas phase. Moreover, an interface sharpening equation is required for this kind of simulation. According to Figure.17, both methods are in correct agreement in terms of bubble break-up. However, slight discrepancies might be seen before the cylinder. As it is an unsteady numerical simulation using 15 millions of cells, results are convincing and attest the correct reconstruction of the wall. To clarify discrepancies, in one hand the wall is

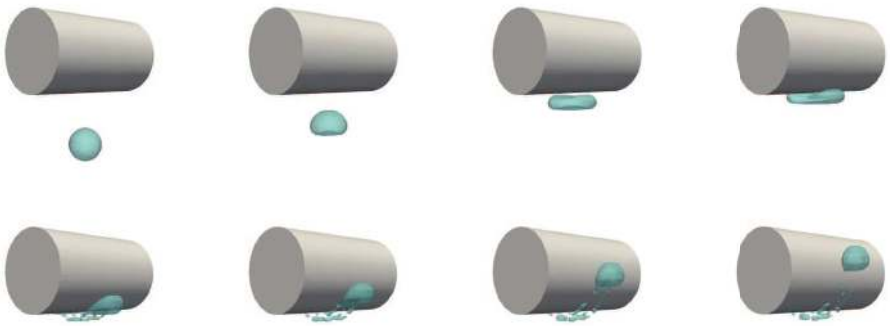

Figure 16. *Snapshots of a bubble impacting a cylinder with the Time and Space Dependent Porosity method at* $t = 0.01,\ 0.1,\ 0.2,\ 0.3,\ 0.4,\ 0.5,\ 0.6,\ 0.7\ s$.

fully reconstructed, on the other a mesh is generated by extrapolation of its nodes; in both cases some errors are introduced which might explain the discrepancies on the figure. It is relevant to specify that interface sharpening and surface tension models which are used in the present study, are developed for cartesian cells only. Consequently, discrete forcing methods are useful for this kind of simulation.

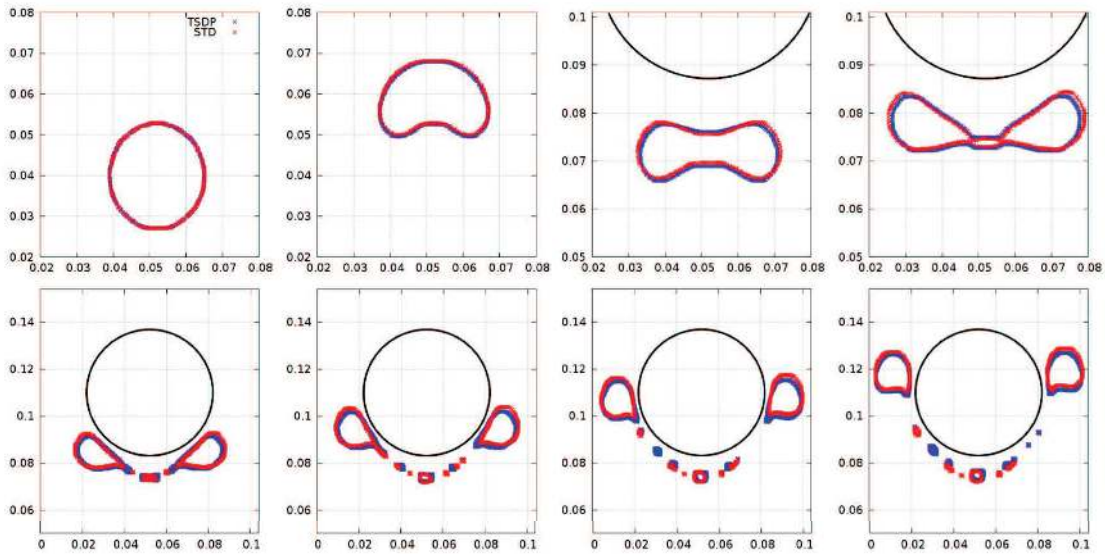

Figure 17. *Contour comparison of a bubble impacting a cylinder between NEPTUNE_CFD with a body-fitted mesh and the Time and Space Dependent Porosity method at* $t = 0.01,\ 0.1,\ 0.2,\ 0.3,\ 0.4,\ 0.5,\ 0.6,\ 0.7\ s$.

4.4. Dam-break on wet bed

The schematic arrangement of the experimental tank [14] is shown in Figure 18. The bottom and side walls are constructed from optically smooth glass, the lock gate is made from plexiglas. The distance of the lock gate is $x_0 = 38\ cm$ in the experiments presented here, the initial water height in the lock is $15\ cm$. Another key parameter is the ambient fluid depth d in the channel before the dam-break: $18\ mm$ and $38\ mm$. The lock gate is opened with a velocity: $v_0 = 1.5\ m/s$.

In this experiment, the water height is measured during $1\ s$ and snap shots are taken. Water coming from the locked tank produces waves because of the progressive opening of the lock.

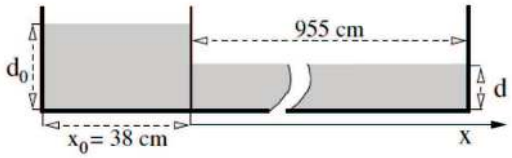

Figure 18. Sketch of the tank.

In the following 2D-simulation, the lock gate is considered as the structure with a velocity v_0. Lock gate and walls are simulated with a slip condition. Results are compared with experimental pictures for $d = 18\,mm$ and with the water height along x for $d = 38\,mm$.

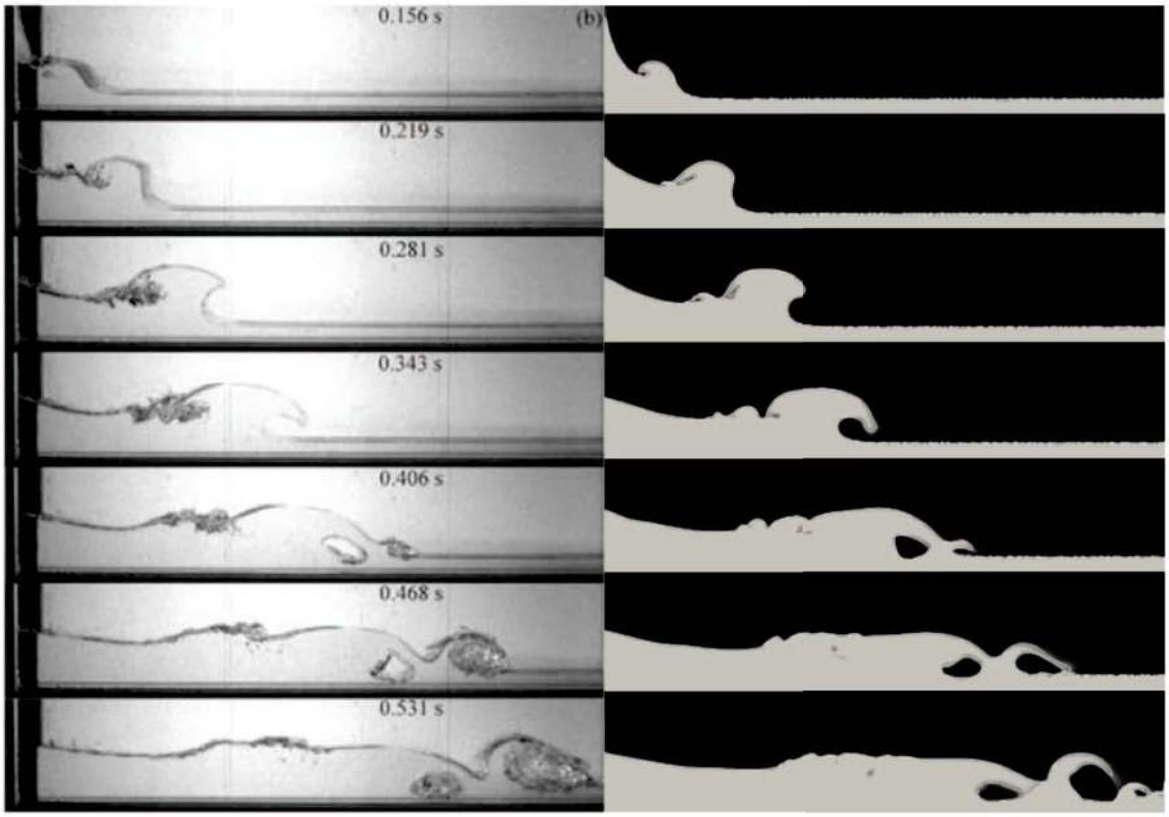

Figure 19. *Experiment/Numerical simulation confrontation of a dam-break on wet bed for* $d = 18\,mm$.

In Figure 19, 7 snap-shots are presented according to the experiment (left) and numerical simulation (right). The position of the free surface can be tracked on experimental records, it is simple to compare with numerical simulation. For different times, results are in agreement with experimental data. Waves are well predicted by the method which allows the conclusion that the Time and Space Dependent Porosity method is a satisfying method in this case.

4.4.1. Paddle A 2D-paddle (presented in Figure 20) is animated by a sinusoidal motion with a velocity:

$$v(t) = 0.15\,\min(1,t)\,cos\left(2\pi t - \frac{3\pi}{2}\right).$$

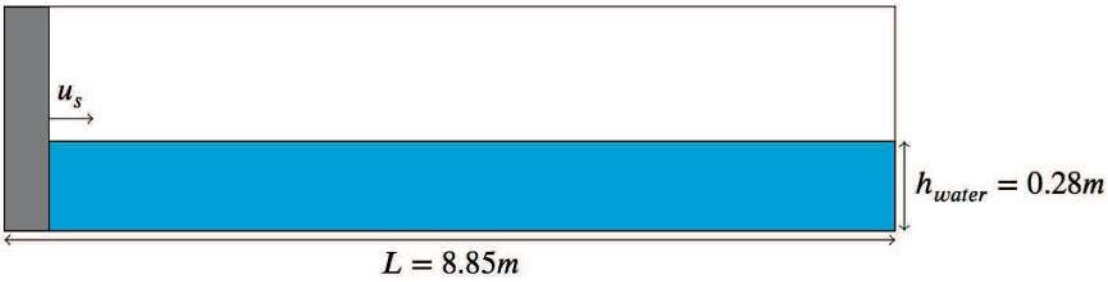

Figure 20. *Geometry of the wave tank case*

In the wave tank, the initial water depth is $h_{water} = 0.28m$ and its length $L = 8.85m$. As the paddle vibrates, waves appear, the free surface consequently moves, its time-fluctuations are recorded in 3 different positions: $x = 0.65\,m$, $x = 3.55\,m$ and $x = 5.45\,m$.

On Figure 21, water height simulation results are compared with experimental data [10] on 2 mesh refinements for 2 positions. First, in front of the paddle, the beginning of the paddle motion

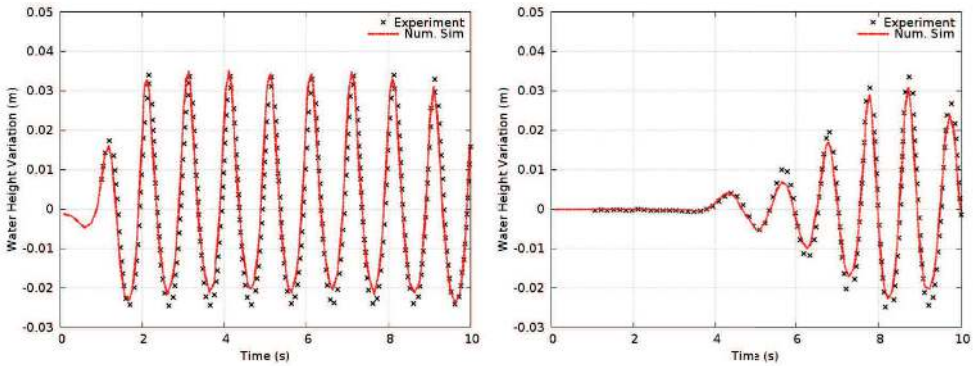

Figure 21. *Free surface evolution for 2 different positions 0.65 m (left) and 5.45 m (right). Comparison between experiment [10] and numerical results from TSDP.*

is well captured by the simulation, there is no phase lag and the height amplitude is correct. For the two others, the wave lag is well predicted, there is also no phase lag but slight differences are present for the height amplitude.

5. DISCUSSION AND CONCLUSION

In the present work, a method to track fluid-structure interface thanks to a discrete forcing method based on a porous media approach is proposed. Implemented in a finite-volume code based on a two-fluid approach called NEPTUNE_CFD [11], the method and the interface reconstruction are detailed. To make the structure moving, a porosity convection is required; this is the key point of the method. Then, each reconstructed or changed item is validated on elementary cases. Finally, the Time and Space Dependent Porosity method is applied to two-phase flow applications. These 3 last simulations lead to reasonable agreements with experimental data despite the solid is moving or not.

In fact, the aim of the method is to reproduce accurately a body fitted mesh on a cartesian grid. Since the numerical method is validated, many future developments are possible with no limitation. In terms of turbulence and wall laws, changes would be in:

- solid-cells: there is no turbulent viscosity generated,

- cut-cells: by considering the new volume, the distance between the cell-center and the porous wall, and the re-computed velocity gradient ; the turbulent terms are changed.
- fluid cells: by defining the distance to porous walls in each cell.

As shown in the validation, forces acting on a structure are well-predicted by the method. It would be now possible to deal with fluid-structure interaction by implementing for example a Newmark algorithm in order to generate the correct displacement based on forces acting on structures. Another possible development is to take into account heat transfers as the solid is meshed. Without external code or mesh, by implementing thermal laws in the porous media, this would reduce the computational time. These steps would allow to work on industrial cases with complex geometries and phenomenon like tube vibrations in steam-generator for example.

ACKNOWLEDGMENT

Authors want to thank both EDF R&D projects: Qual-IFS-GV, devoted to the assessment of SG tube vibration risk; and NEPTUNE funded by EDF (Electricit de France), CEA (Commissariat l'Energie Atomique et aux Energies Alternatives), Framatome and IRSN (Institut de Radioprotection et de Suret Nuclaire).

BIBLIOGRAPHY

REFERENCES

1. J. A. Benek, J. L. Steger, and F.C. Dougherty. A flexible grid embedding technique with application to the euler equations,*AIAA Paper, 83 1944*, 1983.
2. W. Bai, C.G Mingham, D.M Causon, L. Qiand, Finite volume simulation of viscous free surface waves using the Cartesian cut cell approach, *International Journal for Numerical Methods in Fluids 63:69-95*, 2010.
3. Bna. S, Manservisi S., Scardovelli R., Yecko P., Zaleski S., VOFI - Library to initialize the volume fraction scalar field, *Computer Physics Communications 200: 291-299*, 2015.
4. Bn. S, Manservisi S., Scardovelli R., Yecko P., Zaleski S., Numerical integration of implicit functions for the initialization of the VOF function, *Computers and Fluids 113: 42-52*, 2015.
5. D. Clarke, M. Salas, H. Hassan, Euler calculations of multi-element airfoils using Cartesian grids, *AIAA Journal 24: 1128-1135*, 1986.
6. P. Coste, A Large Interface Model for two-phase CFD, *Nuclear Engineering and Design 255:38-50*, 2013.
7. M. Coutanceau, R. Brouard, Experimental determination of the main features of the viscous flow in the wake of a circular cylinder in uniform translation. Part 1 : Steady flow, *Journal of Fluids Mechanics 79: 231-256*, 1977.
8. R. Denfle, S. Mimouni, J.P. Caltagirone, S. Vincent, Multifield hybrid approach for two-phase flow modeling - Part 1: Adiabatic flows, *Computers&Fluids 113:106-111*, 2014.
9. S. Fleau, S. Mimouni, N. Mrigoux, S. Vincent, Validation of multifield approach for the simulations of two-phase flows, *Computational Thermal Sciences 7:441-457*, 2015.
10. F. Gao, An efficient finite element technique for free surface flow, *Ph.D thesis, Brighton University UK*, 2003.
11. A. Guelfi, D. Bestion, M. Boucker, P. Boudier, P. Fillion, M. Grandotto, J.-M. Hrard, E. Hervieu, P.Peturaud., NEPTUNE - A New Software Platform for Advanced Nuclear Thermal-Hydraulics, *Nuclear Science and Engineering 156:281-324*, 2007.
12. M. Bergmann, J. Hovnanian, A. Iollo An accurate cartesian method for incompressible flows with moving boundaries, *Communications in Computational Physics 15:1266-1290*, 20124.
13. Ishii M., Thermo-fluid dynamic, theory of two-phase, *Eyrolles*, 1975.
14. I. Janosi, D. Jan, K.G. Szabo, T. Tel, Turbulent drag reduction in dam-break flows, *Experiments in Fluids 37:219-229*, 2004.
15. Koumoutsakos P., Leonard A. High resolution simulations of the flow around an implusively started cylinder using vortex methods, *Journal of Fluid Mechanics 296:1-38*, 1995.
16. M.J. Lighthill, On displacement thickness, *Journal Fluid Mechanics, 4:383-392*, 1958.
17. N. Merigoux, J. Laviville, S. Mimouni, M. Guingo, C. Baudry, A generalized large interface to dispersed bubbly flow approach to model two-phase flows in nuclear power plant, *CFD4NRS-6 Boston*, 2016.
18. S. Mimouni, F. Archambeau, M. Boucker, J. Laviville, C. Morel, A second order turbulence model based on a Reynolds stress approach for two-phase boiling flow and application to fuel assembly analysis, *Nuclear Engineering and Design*, 2010.
19. R. Mittal, G. Iaccarino, Immersed boundary methods, *Annual review of fluid mecanics*, 2005.
20. L. Morino, M. Gennaretti, and S.F. Shen, Lighthill transpiration velocity revisited: an exact formulation, *Meccanica, 30(2):127-137*, 1995.

21. Noh, A time dependant two-space-dimensional coupled eulerian-lagrangian code, *W.F.alderb edn. Academic Press. 77*, 1964 .
22. C.S Peskin, Flow patterns around heart valves: A numerical method, *Journal of Computational Physics 10(2):252-271*, 1972.
23. K. Taira, T. Colonius, The immersed boundary method: a projection approch, *Journal of Computational Physics 225:2118-2137*, 2007.
24. D.J. Tritton, Experiments on the flow past a circular cylinder at low Reynolds number, *Journal of Fluids Mechanics 22:673-688*, 1959.
25. Y. Tseng, J.H. Ferziger, A ghost-cell immersed boundary method for flow in complex geometry, *Journal of Computational Physics 192:593-623*, 2003.
26. S. Vincent, A. Sarthou, J.P. Caltagirone, F. Sonilhac, P. Fevrier, C. Mignot, G. Pianet,Augmented Lagrangian and penalty methods for the simulation of two-phase flows interacting with moving solids. Application to hydroplaning flows interacting with real tire tread patterns*Journal of Computational Physics 230:956-983*, 2011.
27. S. Wang, X. Zhang, An immersed boundary method based on discrete stream function formulation for two and three dimensional incompressible flows, *Journal of Computational Physics, 230:3479-3499*, 2011.
28. Z. Xie, Numerical study of breaking waves by a two-phase flow models, International Journal for Numerical Methods in Fluids 70:246-268, 2012.
29. T. Ye, R. Mittal, H. Udaykumar, W. Shyy, An accurate Cartesian grid method for viscous incompressible flows with complex immersed boundaries, *Journal of Computational Physics 156:209-240*, 1999.